Proceedings of ASME Turbo Expo 2011
GT2011
June 6-10, 2011, Vancouver, British Columbia, Canada

GT2011-45400

STUDY OF UNFORCED AND MODULATED INCLINED FILM-COOLING JETS USING PROPER ORTHOGONAL DECOMPOSITION – PART I: UNFORCED JETS

Guillaume Bidan **Clementine Vezier** **Dimitris E. Nikitopoulos**

Turbine Innovation and Energy Research (TIER) Center
Mechanical Engineering Department
Louisiana State University,
Baton Rouge, LA, 70803

ABSTRACT

The effects of jet flow-rate modulation were investigated in the case of a 35° inclined jet in cross-flow over a flat plate using Mie scattering visualizations, time-resolved flow rate records and large eddy simulations (LES). An unforced jet study was conducted over a wide range of blowing ratios to provide a baseline for comparison to the pulsed results. The two distinct and well known steady jet regimes (attached jet with high film cooling performance for BR<0.4 and detached jet with poor film cooling performance for BR>1.0) were related to the dynamics of characteristic vortical structures, significant in the transition from one regime to the other. Similarity of the inclined jet results with a past vertical jet study are also put in perspective when comparing wall adiabatic effectiveness results. 3D Proper Orthogonal Decomposition (3D-POD) was performed on LES results of an unforced case at BR=0.15 to provide an analysis of dominant modes in the velocity and temperature fields. Error calculations on the reconstructed fields provided an estimation of the number of modes necessary to obtain satisfactory reconstruction while revealing some of the shortcomings associated with POD.

NOMENCLATURE

D_j	Jet diameter [*mm*]
L	Jet pipe length [*mm*]
X_j, Y_j, Z_j	Normalized coordinates x/D_j, y/D_j, z/D_j
U, V, W	Velocities along x, y and z axis respectively [ms^{-1}]
δ	99% Boundary layer thickness [*mm*]
δ^*	Boundary layer displacement thickness [*mm*]
θ	Boundary layer momentum thickness [*mm*]
H	Boundary layer shape factor
T	Temperature [*K*]
BR	Blowing Ratio
η	Adiabatic effectiveness $(T_{wall} - T_\infty)/(T_j - T_\infty)$
N_r	Number of modes used in POD reconstruction
C_c	Coverage Coefficient $C_c(\eta_x) = 1/A_j \int_{\eta \geq \eta_x} dA_{wall}$

<u>Subscripts</u>

j	Jet
∞	Free stream
span	Spanwise averaged quantity
area	Area averaged quantity

INTRODUCTION

An overshoot of as little as 2% of blade critical temperature can lead to a decrease in the part lifetime of as much as 50%. This simple fact makes blade and vane cooling, and in particular film cooling, an essential feature of modern gas turbine and jet engines. Film cooling systems involve arrays of jets located at the surface of the part to be cooled and supplied through internal cooling channels by cooler air diverted from the compressor. A decrease in the overall amount of air necessary to maintain a certain part temperature could result in lower emissions and/or higher performance (e.g. see [1]).

Multiple attempts at improving film cooling systems have been made following different approaches mostly oriented toward jet hole geometry optimization. State of the art film cooling jets involve complex shaped hole geometries with multiple expansion angles. [2-3] provide a good review of the significant work on passive geometry improvements. One of the major drawbacks of passive systems is found in their lack of adaptability. [4-7] investigated the effects on film cooling of cross-flow unsteadiness such as the one encountered by systems located beyond the turbine first stage. These studies showed that bulk cross-flow pulsations can have a catastrophic effect on cooling performance due to passive jet pulsation, though already detached jets can benefit from unsteadiness. Actively controlled film cooling systems using pulsed jets in cross-flow could provide adaptable jet exit conditions while mitigating the detrimental effects of cross-flow fluctuations.

Acoustically excited or fully modulated jets in cross-flow have been primarily investigated for mixing enhancement purposes. which is detrimental and therefore undesirable for film cooling. In [8-9] modulated jets showed dramatic improvements over their unforced state counter-parts in terms of penetration and mixing rate and, more interestingly for film cooling purposes, spread. However, most of these studies were carried out at blowing ratios well beyond the range encountered in most film applications. The first heat transfer measurements for forced film cooling jets were carried out by [10] using a shower head model with a single cylindrical jet with compound angle and without cross-flow modulation. Their results showed that over the range of considered forcing parameters, the forced jets could provide overall higher adiabatic effectiveness with matching heat transfer coefficients over comparable unforced jets. Shortly after, [11-12] investigated the effects of full modulation of a row of 5 jets over a flat plate on adiabatic effectiveness and heat transfer performance in a steady cross-flow and found that almost all of the forced jet configurations provided lower performance over their unforced counter-parts. In [13], using the same setup coupled with a spoked wheel wake generator, an attempt at counter-balancing large scale cross-flow perturbations lead to the conclusion that forced jets did not provide amelioration of the film cooling performance.

In view of these conflicting results, a simplified flow system involving a single partly modulated jet in cross-flow over a flat plate in laminar cross-flow conditions was studied by [14], focusing on the flow features generated in low blowing ratio forced jets and their impact on film cooling performance. An increase in coverage was observed for a period of time after the jet onset while the effects of cross-flow ingestion at the decrease in blowing ratio significantly affected performance.

The current study carries over the work presented in [14] to a more application-relevant geometry of a 35° inclined modulated jet over a flat plate using reactive Mie scattering visualizations complemented by Large Eddy Simulations (LES) with inlet conditions based on experimentally acquired time resolved jet flow-rate measurements to provide details on the flow and temperature field in the near-field of the jet. 3D Proper Orthogonal Decomposition (3D-POD) of the velocity and temperature fields is carried out to extract statistically relevant information and provide an estimate of the number of modes necessary to reconstruct realistic flow and temperature fields for future development of reduced order models.

This study is presented in two parts, of which the first one deals with the baseline results obtained in unforced conditions. In the first section the different jet regimes are characterized while in the second section, the baseline film cooling results are presented. Finally in the last section, an unforced is analyzed using 3D-POD. Part II [15] of the study presents the results obtained with the forced jets and offers interpretations in the perspective of the unforced results when appropriate.

EXPERIMENTAL AND NUMERICAL SETUP

The experiments were conducted in an open loop wind tunnel, a schematic of which is presented in Fig. 1, with a 3m long test section and a 0.9mx0.6m cross section. Optical access was available through a pair of transparent acrylic walls constituting the top and one of the side walls of the test section, respectively allowing visualizations in planes parallel to the bottom wall (X-Y) and along the jet symmetry plane (X-Z). The flow in the test section was laminar (free stream turbulence intensity <0.5%), with a boundary layer Reynolds number at the jet level of $Re_\delta=U_\infty.\delta/\nu=1{,}710$. In this more fundamental study aimed at the observation of the vortical structures generated under pulsed conditions, the choice of laminar boundary layer was made in order to limit the number of factors affecting the jet behavior.

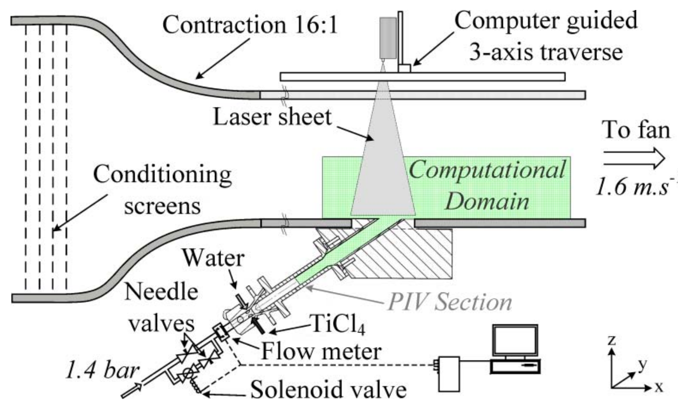

Figure 1 – Experimental setup.

The jet exited from a 25.4mm round tube mounted flush to the bottom wall at an angle of 35° with respect to the cross-flow direction and zero compound angle. The air supply for the jet was provided by an industrial compressor, dried and regulated at 1.4bar. An in house seeding system injected water and Titanium Tetrachloride ($TiCl_4$) vapors at two locations inside the jet pipe to generate Titanium Dioxide (TiO_2) particles used as a tracer for Mie scattering visualizations in the experiments.

The tube length to diameter ratio effects have been substantially studied by [16], [17], and [18] for instance and reveal that longer feeding tubes lead to better performance than shorter ones by decoupling the blade internal channel flow from the external flow and preventing the jetting of the coolant. A threshold has been observed in a previous study ([18]) where performance is constant for $L/D_j>7$. Therefore, the jet pipe was set to $12D_j$ to also allow for flow development, reduction of perturbations introduced by the seeding system, and allow for homogenous seed mixing.

Laser sheet reactive Mie scattering visualizations, hotwire anemometry and time resolved flow-rate measurement were the principal methods used during experiments and were handled through A/D converters to allow synchronized acquisition and actuation. Flow-rate records were acquired at 1 kHz.

Numerical simulations were carried out in parallel to the experiments to provide additional information on the vortical structures formed under unforced and forced conditions. Fluent[tm] was used to simulate the unsteady, turbulent flow through an incompressible Large Eddy Simulation (LES) model directly using a dynamic Smagorinsky sub-grid scale model.

Figure 2 shows the simulated domain and boundary conditions consisting of a rectangular box representing a part of the wind-tunnel test section used in the experiments and part of the jet feeding tube.

Table 1 – Inlet boundary layer characteristics at X_j=-6, Y_j=0

U_∞	δ/D_j	δ^*/D_j	θ/D_j	H
1.6 $m.s^{-1}$	0.630	0.172	0.077	2.23

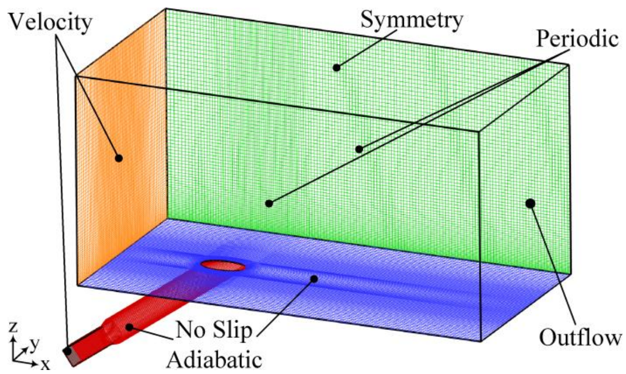

Figure 2 – LES domain and applied boundary conditions.

The computational domain was 18D_j long (x-direction), 8D_j wide (y-direction) and 6D_j tall (z-direction), respectively discretized into 160x100x90 hexahedral cells, while the pipe feeding the jet was taken 8D_j long, discretized by 2000 nodes in the cross-section and 120 nodes in the axial direction. Overall the mesh used was structured and counted 1.6 millions cells. The jet exit center was located 6D_j downstream from the domain inlet. The first cells in contact with the walls were approximately 0.02D_j tall, yielding average y^+ values of order of one thus reaching the viscous sub-layer and allowing direct solving of the wall shear stress from laminar stress-strain relationship, without using wall functions. Velocity characteristics and boundary layer profiles for the inlet of the computational domain were obtained from hotwire measurements performed in the wind tunnel as summarized in Table 1. The numerical solver used was pressure based with second order accuracy in time and space. The time steps used ranged from 5.10^{-5}s at BR=1.2 to 5.10^{-4}s at BR=0.15 in order to be under the minimum Kolmogorov time scale in the domain. Several thousands of iterations were necessary to obtain statistically relevant data accounting for more than 50 hours of computation for each case on high performance computing platforms under the Louisiana Optical Network Initiative (LONI) at Louisiana State University (IBM Power5+ at 1.9GHz), using an average of 24 processors per run. At the inlet of the jet pipe, uniform velocity profile was set so as to equal the volumetric flow rate of the experiment. The jet and cross flow fluids were maintained at constant temperature of respectively 300 and 330K, not affecting the velocity field.

A series of constant temperature anemometry measurements were performed at blowing ratios of BR=0.150 and BR=1.0, at 4 different streamwise locations (X_j=0, 2, 5, 9) and are presented in Fig. 3 along with extracted corresponding simulation results. Overall the LES results compare reasonably well with the experimental measurements at all streamwise locations and for both blowing ratio cases with exception of the measurement at BR=1.0 and X_j=2 where the LES results somewhat under predict the velocity. These results, along with the qualitatively good agreement between experimental and numerical visualizations shown in the next sections provide good confidence in the LES results obtained for the purposes of this study.

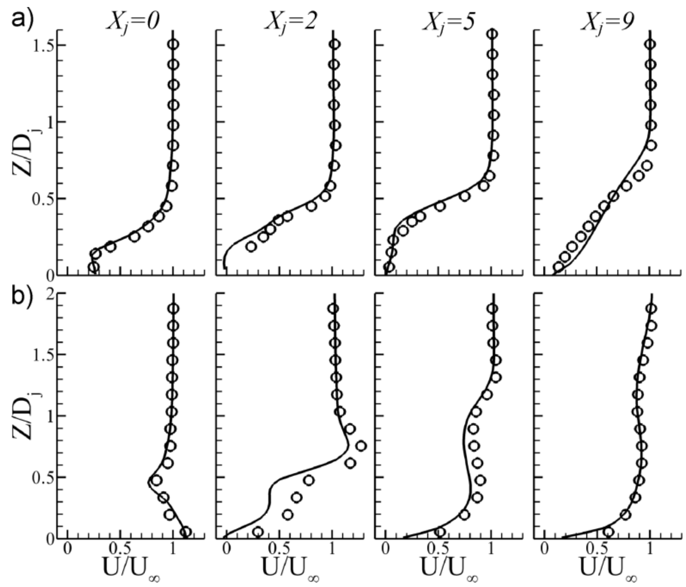

Figure 3 – Experimental (*symbols*) and LES (*solid line*) time averaged streamwise velocity profiles at a) BR=0.150, b) BR=1.0 at X_j=0, 2, 5 and 9.

RESULTS AND DISCUSSION

In steady state experiments the jet was studied using reactive and fully reacted Mie scattering visualizations. Selected cases at BR=0.15, 0.3, 0.4, 0.75, 1.0 and 1.2 were simulated using LES.

Jet Regimes

In the same way as the vertical jet in cross-flow described in [14], several unforced jet regimes were observed. At low blowing ratios under 0.4 the jet was fully attached to the wall while at blowing ratios above 1.0, the jet was completely detached. At intermediate blowing ratios, the jet exhibited vortical structures from both types of regimes.

The attached jet is the most relevant configuration to film cooling and shows strong similarities with the vertical jet configuration. The dominant shear layer vortical structures consist in interlocked hairpin vortices observed in the experimental side-views of Fig. 4a as well as the LES results of Fig. 7 at BR=0.15. These vortices are developing as the result of a Helmholtz-type instability in the jet shear layers and have been observed in previous studies such as [19]. In the experimental case at BR=0.15, the instability seems to develop faster in the upper shear layer which is where the initial rollup occurs first. Eventually both upper and lower shear layers merge a few diameters downstream of the jet exit and the hairpin vortex is fully formed.

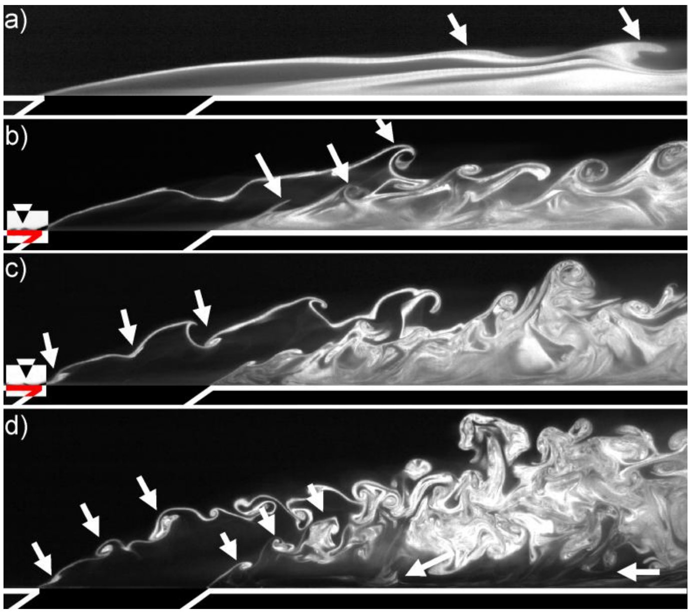

Figure 4 – Experimental Mie scattering visualizations in the plane Y_j=0 at a) BR=0.15; b) BR=0.4; c) BR=0.75; d) BR=1.1.

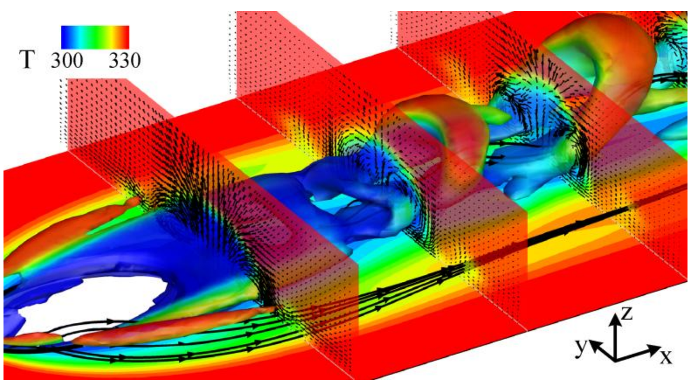

Figure 5 – Laplacian of the pressure iso-surfaces at BR=0.300 from LES and instantaneous wall temperature.

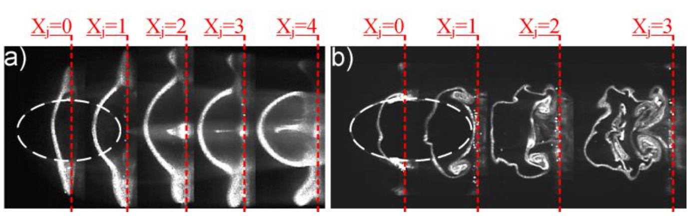

Figure 6 – Experimental Mie scattering visualizations on a plane inclined at -30° with respect to the Y-Z plane for a) BR=0.15; b) BR=0.75.

As the blowing ratio is increased, a coupling between upper and lower shear layers fluctuations occurs so that eventually at BR=0.4, both shear layers exhibit distinct rollups, each corresponding to a hairpin vortex, merging as they are convected downstream as evidenced in Fig. 4b. As seen in Fig. 5 and Fig. 7, the shear layer vortical structures have a strong influence on the wall temperature field as they carry most of the coolant fluid from the jet while generating a velocity field responsible for entraining cross-flow fluid into the wall region. The dynamics of the hairpin vortices are comparable to those observed for the vertical jet and are dictated by cross-flow convection as well as mutual, self, and mirrored induction with respect to the bottom wall. While the convection caries the structures downstream, the mutual induction of one leg onto the other creates a positive vertical velocity component entraining the hairpins legs away from the wall. In the meantime, the induction from the mirrored image of the legs with respect to the bottom wall generates a spanwise motion toward the symmetry plane (Y_j=0) pushing the legs toward each other and consequently reinforcing the induced upward motion as the distance between the vortex cores is decreased. Similarly, the mirrored induction on the head of the hairpin vortices as well as the self-induction of the curved vortex line result in a backward/upward motion for the hairpin head. As a result of those combined inductions, the hairpin vortices and the coolant are carried away from the wall within a few jet diameters downstream of the jet exit thus breaking the film coverage and entraining cross-flow fluid near the wall. As the blowing ratio is increased, the hairpin vortices legs gain in strength and tend to detach earlier from the wall and entraining more cross-flow fluid near the bottom surface. This is observed in the reactive Mie scattering visualizations of Fig. 6 where at BR=0.15 (Fig. 6a) the legs of the hairpin vortices lift-off between X_j=3 and X_j=4, whereas at BR=0.75 (Fig. 6b) the legs are completely detached beyond X_j=1. As the legs detach, a significant amount of reacted seed can be observed underneath the jet core, resulting from the mixing of jet seeded fluid and moist cross-flow fluid, thus entrainment. Figure 7a through 7d show the impact of the hairpin vortices lift-off and consequent cross-flow entrainment on the adiabatic wall temperature.

Directly downstream of the jet exit in Fig. 4a as well as Fig. 6a, a region of reacted seed evidences the characteristic recirculation region encountered in the attached jet configuration. This region, principally supplied by jet fluid, is also observed in the LES results and corresponds in Fig. 7a and 7c to an area of lower temperatures encompassed by the hairpin vortices legs. Upstream of the jet exit, the horseshoe vortex appears to be absent from the side visualizations of Fig. 4a at the lowest blowing ratios, as well as from the LES results of Fig. 7a, although a pair of streamwise vortices coherent with the horseshoe vortex develops on the sides of the jet without connecting upstream in the usual horseshoe U shape. These streamwise vortices are also identifiable in the experimental visualizations of Fig. 6a on each side of the jet as they carry reacted particles. The absence of a full horseshoe vortex was already documented in previous studies such as [19] and [20] in cases where the cross-flow blockage due to the presence of the jet was weak which is clearly the case here at such low blowing ratios and with an inclined jet. Yet, the presence of the jet forces a cross-flow deflection and generates a spanwise velocity gradient in the vertical direction at the origins of the side vortices near the jet exit. In Fig. 5 the streamlines show that jet fluid exits very close to the wall and on the sides of the jet and provides significant wall coverage as seen in the adiabatic effectiveness contours of Fig. 7a and 7c. As the blowing ratio increases, so does the jet blockage, so that at BR=0.4 in Fig. 4b (tail-less arrow) and 7c, a complete horseshoe rollup is formed ahead of the jet and carries jet fluid. Further downstream, longitudinal streamwise vortices develop on each side of the hairpin vortices which combined with the previously mentioned side vortices appear as a set of X patterned structures laying near the bottom wall. These were also observed in the vertical jet configuration of [14] and were dominant in the far field. One of the main differences between the two configurations is the absence of flow separation and stable upper shear layer rollup inside the jet pipe of the inclined jet. The interaction between the inner vortex and the horseshoe vortex in the 90° injection configuration was responsible for significant coolant entrainment in the upstream region of the jet exit, not observed in the current 35° configuration.

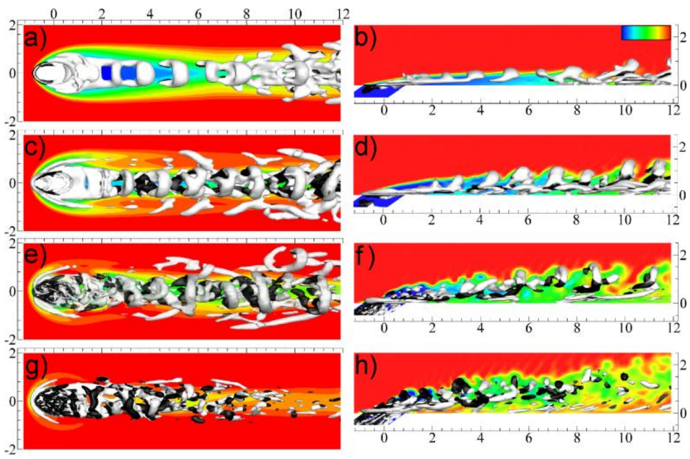

Figure 7 – Laplacian of the pressure iso-surfaces from LES colored with spanwise vorticity contours (*black: negative, white: positive*) at a-b) BR=0.15; c-d) BR=0.4; e-f) BR=0.75; g-h) BR=1.2 and instantaneous temperature contours in the planes Z_j=0 (l*eft*) and Y_j=0 (*right*).

As the blowing ratio is increased beyond BR=0.4, rollups with negative spanwise vorticity start to form in the upper shear layer as seen in the experiments in Fig. 4c as well as in the LES results of Fig. 7f for BR=0.75. Overall, downstream of the jet exit, rollups with positive spanwise vorticity still develop in the upper shear layer, thus the dominant vortical structures remain hairpin vortices. However, as mentioned earlier, the increased vorticity in the legs and initial vertical momentum at the jet exit triggers significant lift-off, directly impacting the film cooling coverage as seen in Fig. 7e. Organized motion taking the form of two counter-rotating vortices underneath the jet core appear to develop as the large rollups of Fig. 6b suggest. At BR=0.75 where the fluctuation levels are significantly higher than the lower blowing ratio cases, multiple scales of shear layer structures develop at the jet/cross-flow interface as seen in Fig. 6b where smaller kidney/anti-kidney vortices develop along with the larger scale counter-rotating pair. Such multiplicity of the shear layer structures have been previously documented by [21] for instance. It should be noted that the side vortices observed at lower blowing ratios are still present at BR=0.75 as seen in Fig. 7e with apparently stronger coherence.

For BR≥1, the jet exhibits the principal jet in cross-flow structures extensively documented at high BR values for the vertical jet (see [22-23]). Rollups of negative spanwise vorticity are consistently formed in the upper shear layer as evidenced in Figs. 4d and 7g, as well as tornado-like wake vortices located below the jet core carrying jet fluid since they are seeded by particles. A complete, yet rather short, horseshoe vortex is observed in the LES results of Fig. 7g, although not in the experimental visualizations due to the absence of seed, indicating that the horseshoe vortex does not entrain jet fluid.

Film Cooling Performance

Quantitative information was extracted from the numerical simulations to provide a performance benchmark to the forced results and was also compared to the vertical jet results. Figure 8 presents time-averaged wall adiabatic effectiveness for the inclined jet. At BR=0.15, (Fig. 8a), the area of high adiabatic effectiveness directly downstream of the jet exit corresponds to the recirculation region enclosed by the legs of the successive hairpin vortices. As mentioned previously, significant cooling is brought to the wall by jet fluid exiting on the sides of the jet, which will further downstream generate the side-vortices. As the blowing ratio is increased, the side-vortices become more coherent and tend to lift off the wall closer to the jet exit evidenced by the pair of traces along the jet core. From BR=0.15 to BR=0.4 a relative increase in spread is observed for X_j≥7 due to the beneficial effect of the side vortices and their favorable velocity field. As the jet enters the transition regime (0.4<BR≤0.9), the wall coverage downstream of the hole is degraded though more homogeneous, and becomes marginal in the detached configurations where the jet wake is the only region showing a decrease in temperature.

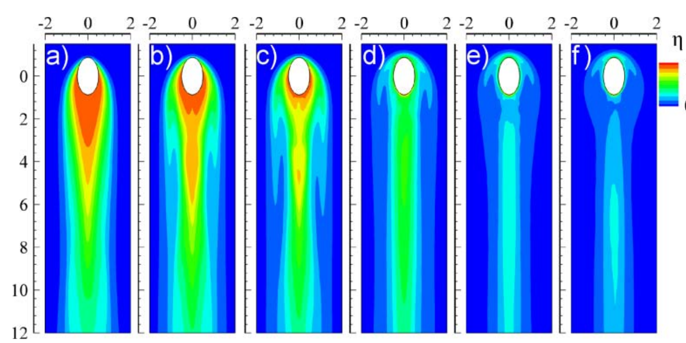

Figure 8 – Wall adiabatic effectiveness contours from LES at a) BR=0.15; b) BR=0.3; c) BR=0.4; d) BR=0.75; e) BR=1.0; f) BR=1.2.

Figure 9 presents downstream spanwise averaged adiabatic effectiveness as well as center line adiabatic effectiveness and comparable results from the vertical jet. In Fig. 9a, directly downstream of the jet exit (X_j<6), the case at BR=0.15

performs better due to the presence of the steady recirculation region fed by jet fluid. However further downstream (X_j>6) the case at BR=0.3 provides increased adiabatic effectiveness due to the increased coolant flow rate and spread over the case BR=0.15. As the blowing ratio increases beyond 0.3, the spanwise averaged performance of the inclined jet decreases continuously. The centerline results for the inclined jet in Fig. 9b show similar trends. The local decrease in $\eta_{centerline}$ observed for BR≥0.3 directly downstream of the jet exit is due to early lift-off of the shear layer vortices, allowing cross-flow penetration in the vicinity of the jet exit. For BR≤0.3, the inclined jet shows greater spanwise averaged as well as center line adiabatic effectiveness compared to the vertical jet. However the inclined jet performance is degraded beyond BR=0.3 which was not the case for the vertical jet the performance which continued increasing up to BR=0.415. Thus at BR=0.4 the vertical jet exhibits greater η_{span} values than the inclined configuration. At higher blowing ratios (BR≥0.75), the inclined jet performs better than the vertical jet as is well known to do so. The $\eta_{centerline}$ trends show that the inclined jet always provides greater center-line effectiveness over the vertical jet. This indicates that the overall better performance of the vertical jet at BR=0.4 comes mainly from a greater spanwise spread of the coverage (see [14]).

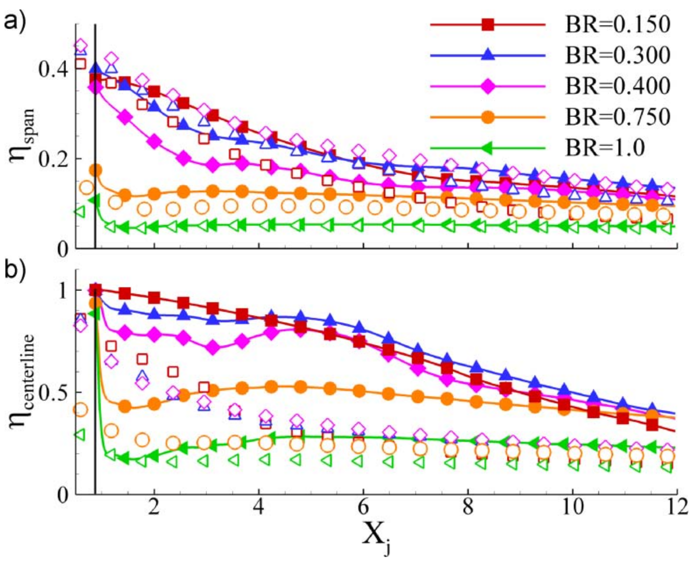

Figure 9 – a) Spanwise averaged adiabatic effectiveness and b) center line adiabatic effectiveness from LES for the inclined jet (*solid line, filled symbols*) and the vertical jet (*open symbols*).

Figure 10 presents area-averaged adiabatic effectiveness and coverage coefficient (wall area over which the adiabatic effectiveness is at a value above a set threshold normalized by jet exit area) for both inclined and vertical jets, giving a single figure global performance index at every blowing ratio. The η_{area} trend of Fig. 10a for the inclined jet exhibits a constant decrease in performance past BR=0.3 with a slight improvement from BR=0.15 to BR=0.3. This result is consistent with the previous observations on η_{span}. According to Fig. 8a, the improvement from BR=0.15 to BR=0.3 corresponds to an increase in η values beyond X_j=5. A local maximum is expected to exist between BR=0.15 and BR=0.3 which is rather low for an inclined jet configuration and is explained by the use of laminar cross-flow conditions. The comparison with the vertical jet results shows that the expected performance degradation as the blowing ratio increases is less abrupt in the inclined configuration than in the vertical setup. Interestingly, the vertical jet performs better at BR=0.415 with an area averaged adiabatic effectiveness of 0.225 within the considered field of view (-1.2<X_j<12). The coverage coefficient trends in Fig. 10b confirm the above mentioned results with a consistent decrease in performance from BR=0.3 for the inclined jet. The comparison with the vertical jet shows that the inclined jet provides more coverage at high effectiveness (η≥0.5) than the vertical one. The vertical jet though provides significantly greater coverage at lower effectiveness levels (almost double in some cases), sign of a greater spread at higher injection angle. Higher spread and performance in the neighborhood of the jet exit (X_j<12) for high injection angles were previously reported in studies such as [24].

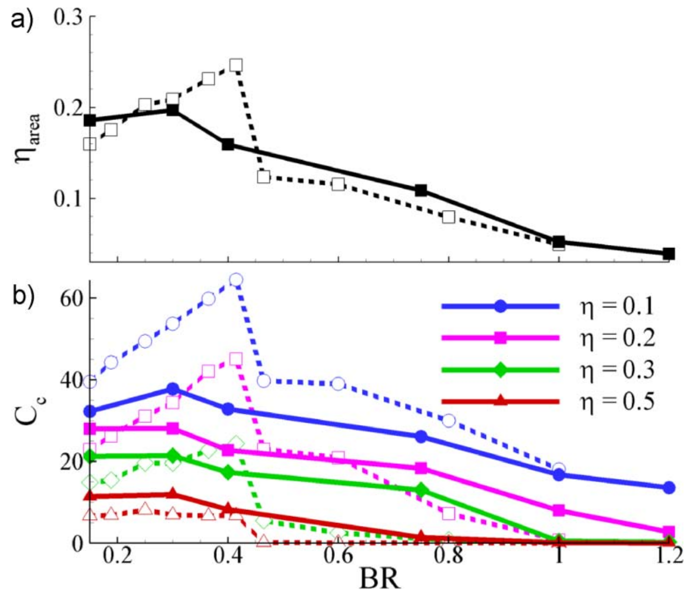

Figure 10 – a) Area averaged adiabatic effectiveness for the inclined jet (*solid line*) and the vertical jet (*dashed line*) and b) coverage coefficient for thresholds η=0.1, 0.2, 0.3, 0.5.

The overall greater performance of the vertical jet in this study should be put in perspective with respect of two considerations. First, the domain of the current study was limited to the near field (X_j<12), which in [24] is approximately the streamwise location beyond which the inclined jet starts to have better performance than the vertical one, and is not taken into account in the results of Fig. 10. Also, it was explained in [14] that the sudden decrease in performance in the 90 degrees injection configuration was to be attributed to a destabilization of the inner vortex formed inside the jet tube, extremely

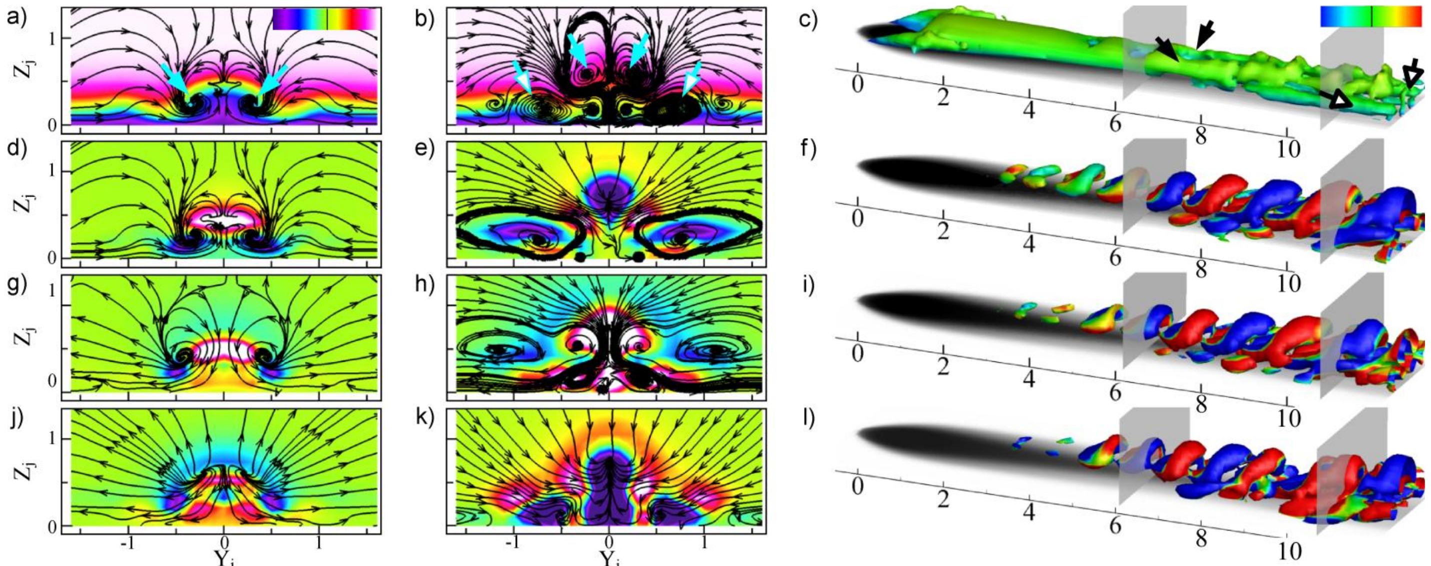

Figure 11 – Mean flow (0th POD Mode) and first 3 velocity POD modes at BR=0.15 a-c) Mode0; d-f) Mode1; g-i) Mode2; j-l) Mode3. Slices at X_j=6 (*left*), X_j=10.6 (*center*) with U velocity contours and V-W streamlines. Q-Criterion iso-surfaces (*right*) computed from the corresponding POD modes colored by U velocity and mean wall temperature contours (*grey scale*).

sensitive to both cross-flow and jet inlet conditions. Hence, it is expected that outside the laminar cross-flow boundary layer conditions used in this study, the transition could happen significantly sooner in the vertical jet while not affecting the inclined jet as much leading to better performance of the latter.

POD Analysis

Proper orthogonal decomposition (POD) has been recently used in fluid dynamics to provide a statistical modal decomposition of a flow field, maximizing the kinetic energy contained in each mode while providing an orthogonal basis conserving general properties such as divergence free for incompressisble flows… Hence POD has become one of the prefered methods to provide a simplified decomposition of flow the dynamics through the most energetic modes in order to analyze dynamically complex and unstable flow configurations such as open cavity flows as in [25], supersonic jets in [26] and also transverse jets in [27-29] in view of providing low order models for flow control. In the current study, the 3D flow field and temperature field from LES at BR=0.15 were analyzed using the POD snapshot algorithm method first described in [30]. A set of 200 statistically independent flowfields and temperature fields with a spatial density of 10 points per jet diameter were used. It was found that at the considered low turbulence levels, 300 snapshots and 20 vectors per jet diameters lead to sensitively identical results with yet considerably longer computation times. The analyzed sub-domain was such as $\{-1\leq X_j\leq 12,\ -2\leq Y_j\leq 2,\ 0<Z_j\leq 2\}$ yielding 106,600 spatial points at the lowest resolution.

Figures 11a-c, 12a and 13a show slices of the first four velocity POD modes (including the mean flowfield) as well as the corresponding Q-criterion (2nd invariant of the velocity divergence tensor) iso-surfaces. The time averaged flowfield exhibits the classical features of inclined jet in cross-flow and

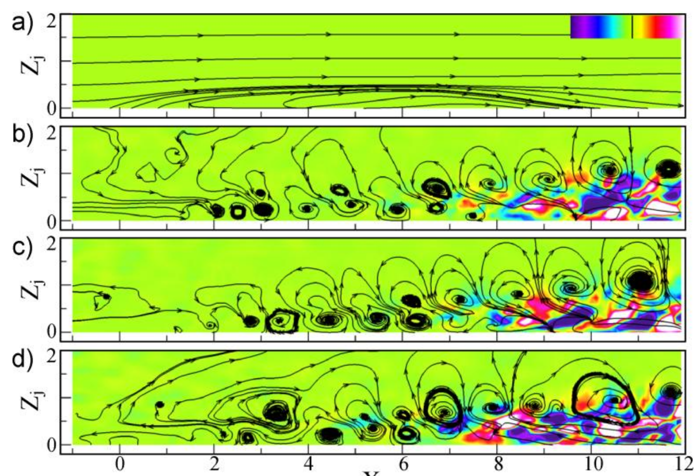

Figure 12 – Mean flow and first 3 velocity POD modes at BR=0.15 a) Mode0; b) Mode1; c) Mode2; d) Mode3. Slices at Y_j=0 with V velocity contours and U-W streamlines.

compares qualitativelly well with previously reported results [31]. In particular the presence of a pair of counter-rotating vortices (CRVP) is visible in the X_j=6 and 10.6 slices (solid arrows) as well as in the Z_j=0.25 slice with upward motion arround the Y_j=0 line surounded by two lines of downward motion at $Y_j=\pm0.5$. The CRVP is generated through the downstream convection of the shear layer hairpin vortices legs. In addition at X_j=10.6 a secondary pair of counter-rotating streamwise vortices (hollow arrows) of opposite vorticity is formed near the wall on each side of the jet, corresponding to the side vortices observed in Fig. 7. The side vortices are observed in Fig 11c for $X_j>9$ and are materialized in the average flowfield by vortex tubes along the jet core as well as in Fig. 13a through the formation of another 'stripe' of positive vertical motion at $Y_j=\pm0.9$. The side vortices have a positive impact on the temperature field at the wall in Fig. 7 as the lateral spread increases marginally beyond X_j=9. The mutual induction between CRVP and side vortices also generates a downward velocity component opposite to the one generated by the interaction between left and right CRVPs thus delaying the lift-off of the jet core from the bottom wall.

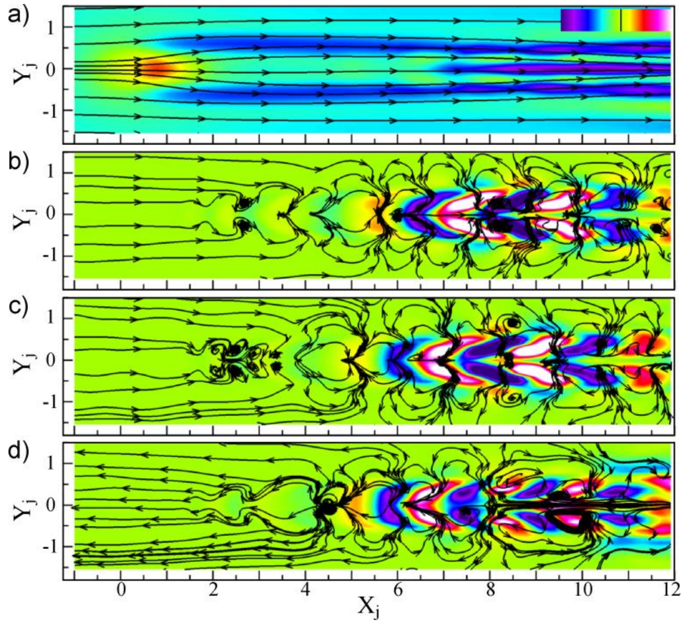

Figure 13 – Mean flow and first 3 velocity POD modes at BR=0.15 a) Mode0; b) Mode1; c) Mode2; d) Mode3. Slices at Z_j=0.25 with W velocity contours and U-V streamlines.

The remaining POD modes provide an orthogonal decomposition of the fluctuation part of the velocity. According to Fig. 14a, the first two POD modes virtually capture the same amount of energy whil being also very similar in shape when comparing Fig. 11f and 11i, Fig. 12b and 12c as well as Fig. 13b and 13c with yet a 'phase shift' in the streamwise direction. Both modes exhibit alternating changes in the sign of the velocity components in the downstream direction. Hence, the cummulative effects of Mode1 and 2 alternating positive and negative velocity regions combined with the phase shifted variations in the signs of a_1^{Vel} and a_2^{Vel} generates a downstream motion. This result is typical of flows dominated by the convection of vortical structures as explained in [28, 32]. In the present case, this behavior is associated with the convection of the shear layer hairpin vortices which are the principal structures observed in the attached jet configuration, supported by the fact that Figs. 11f and 11i show Q-criterion iso-surfaces very similar to the one of hairpin vortices observed in Fig. 5 and 7a. The velocity vector field associated with the first two POD modes also exhibits in Fig. 13b and 13c focus points corresponding to the hairpins legs. It is also observed that the first modes are strong rather far away from the jet exit but not particularly significant near the jet exit. This is explained by the fact that proper orthogonal decomposition 'sorts' the modes with respect of the amount of kinetic energy they contain, thus sorting the scales of the structures as well, such that the most energetic modes (first modes) will usually represent the largest structures. The third mode presented in Fig. 11k-m, 12d, 13d exhibits similarities with the first two modes with alternating positive and negative vertical velocity in the plane Z_j=0.25, though the pattern appears less regular. In the plane Y_j=0 of Fig. 12d, the streamlines clearly show the formation of rollups in the jet upper shear layer. A strong negative streamwise velocity region is located near the symmetry plane (Y_j=0) between the hairpin legs which is visible in the plane X_j=10.6 as well. While streamwise vorticity from the fluctuations of the CRVP and side vortices is captured in the first two modes, no significant x-vorticity appears to be contained in the third mode at X_j=6 or 10.6. Although according to Fig. 14a several other modes appear to carry a significant amount of energy, they will not be presented in the current document for the sake of brevity. However, it should be noted that the forth mode resembles closely the third one yet with a 'phase shift' in the same way the first and second modes were related. The additional modes (N≥5) describe principally the dynamics of the near-wall region, particularly the side vortices and their interaction with the hairpin vortices.

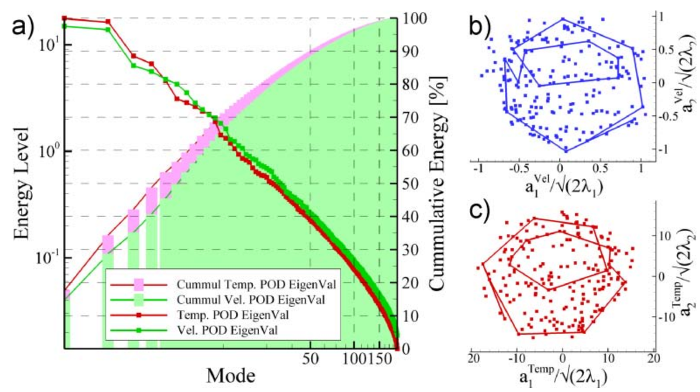

Figure 14 – POD decomposition metrics for BR=0.15 a) POD modes eigenvalues and cummulative temperature and velocity energies b) First two velocity POD coefficients; c) First two temperature POD coefficients.

The temperature field was analyzed as well using POD. Although the norm used in the standard proper orthogonal decomposition does not maximize the thermal energy, this method has been used in previous work to provide a set of orthonormal functions that can be used to obtain a reduced order model of the temperature field ([33-34]). However, it can be argued that the decomposition may not be as 'optimal' as the one obtained for the velocity field in terms of energy since its associated norm is not related to any measure of the internal energy, but only the "energy" of the temperature signal.

The 0^{th} mode (average temperature field) is presented in Fig. 15a-c, 16a, 17a. The temperature field at the wall (Fig. 17a) is consistent with the one presented in Fig. 8a. The contours in Fig. 15a and 15b show the averaged impact of the CRVP and the side-vortices on the temperature field. While the CRVP entrains hot cross-flow fluid near the wall, the side-

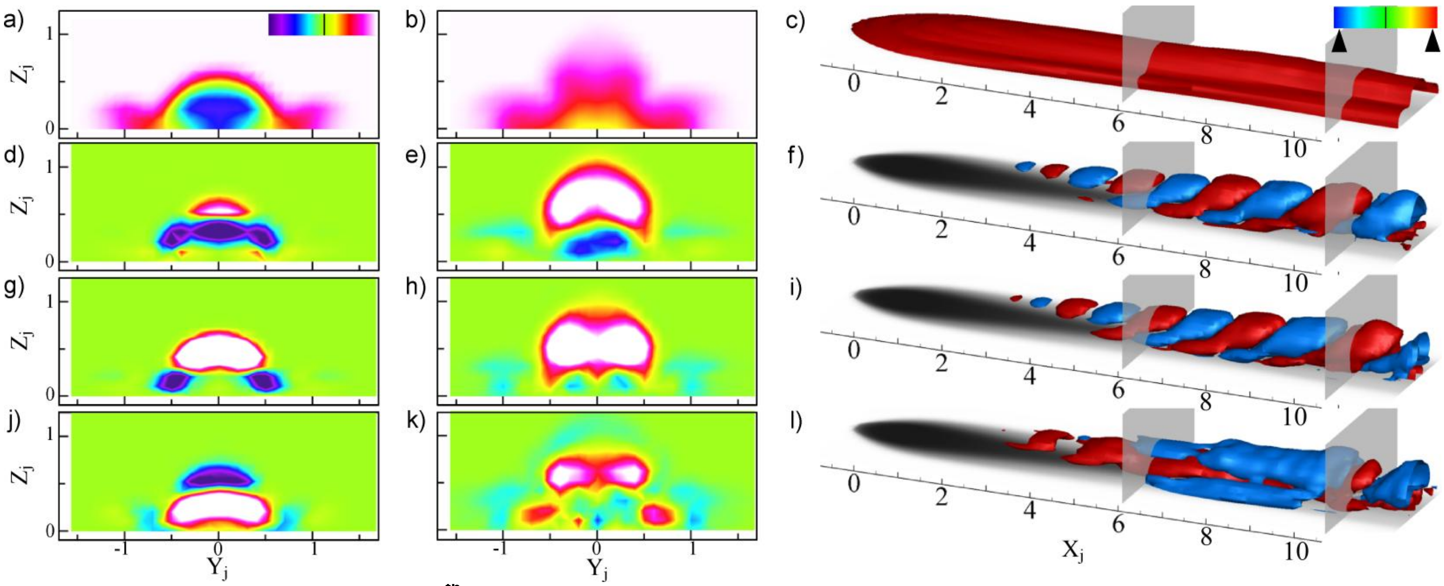

Figure 15 – Mean temperature field (0th POD mode) and first significant temperature POD modes at BR=0.15 a-c) Mode0; d-f) Mode1; g-i) Mode2; j-k) Mode5. Slices X_j=6 (*left*), X_j=10.6 (*center*) with temperature contours. Iso-temperature surfaces (*right*) computed from corresponding POD modes (*red: positive blue: negative*) and mean wall temperature contours (*grey scale*).

vortices tend to increase the spread by carying jet fluid away from the jet core as the two lumps of cooler fluid at $Y_j=\pm1$ suggest. In Fig. 14a, the two first modes carry equivalent 'temperature signal energy' while Figs. 15f and 15i show that both modes, related to the hairpin shear layer vortices according to the shape of their iso-surfaces, are overall identical with a phase shift in the streamwise direction. Based on these considerations and given the distribution of the phase diagram in Fig. 14c showing alternating signs for a_1^{Temp} and a_2^{Temp}, it appears clearly that the first two modes describe the convective effect of the hairpin vortices on the temperature field. Near the wall at $Z_j\approx0$ (Fig. 17b,c), the two modes exhibit similar shifted patterns yet a noticeable difference exists near X_j=10 with the presence in the second mode of a pair of patches with a negative value (*dark*) on each side of the jet (around $Y_j=\pm1$) which counterpart is not clearly found in the first mode. A comparable discrepancy between the two first modes is found in the same plane around X_j=8, where in Mode1 a pair of patches of rather high positive values (*white*) near $Y_j=\pm1$ are present yet no equivalent counter part is found in Mode2. These differences can be attributed to 'quasi-stationary' events occuring near the wall where the velocity is low and the convective effects are not as strong. Thus, while the positve patches in Mode1 appear to correspond to the effect of the hairpin vortices on the pinching of the jet coverage observed in the mean teperature field and attributed to cross-flow entrainment from the legs of the structures, the negative patches in Mode2 are likely to be associated to the spreading of the jet coverage due to the effects of the side vortices. For the sake of brevity, the 3rd and 4th modes are not presented here as they appeared very similar to the two first modes and were as well associated with the convective effects of the hairpin shear layer vortices although at smaller length scales.

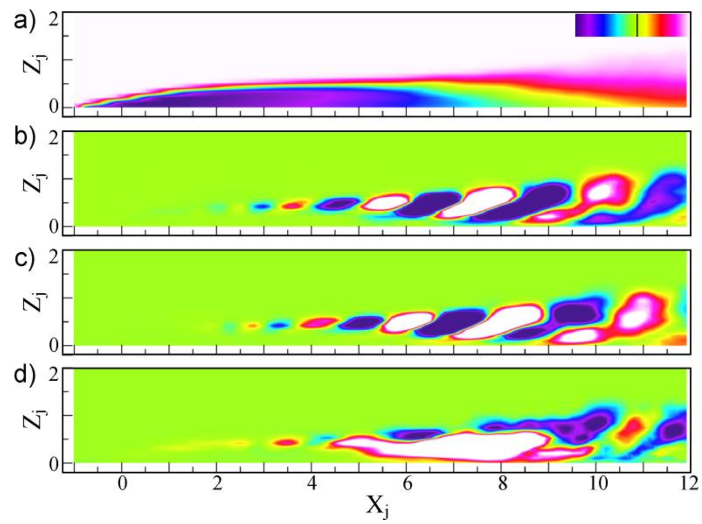

Figure 16 – Mean temperature field and first significant temperature POD modes at BR=0.15 a) Mode0; b) Mode1; c) Mode2; d) Mode5. Slices Y_j=0 with temperature contours.

The 5th mode, however associated with a lower eigenvalue (Fig. 14a), captures a different behavior as shown in Fig. 15k-m, Fig. 16d and Fig. 17d. At X_j=6 and X_j=10.6, Mode5 exhibits two continuous zones in the streamwise direction with positive and negative values. This mode appears to capture a different type of mixing since conversely to Mode1 and 2 the spatial distribution of the mode is not alternating signs in the downstream direction and no other POD mode was found to assume a similar distribution. These observations suggest Mode5 is associated with the mixing behavior induced by the CRVP rather than the downstream convective effect of the hairpin vortices. Hence, the stacking of an area with negative values on top of one with positive values can be interpreted by the CRVP bringing cooler fluid to the upper part of the domain while entraining hotter fluid near the wall and toward the symmetry plane. Near the wall in Fig. 17d, a large area of negative values is visible around X_j=8, Y_j=±0.5 where the jet coverage starts to degrade due to cross-flow entrainment. A similar distribution was found near the wall in Mode4 although the rest of the distribution was more consistent with the Mode3. From these observations, it can be argued that the temperature POD modes are more correlated than the velocity modes and part of the information associated with specific phenomena can be captured across several modes.

Figure 14a provides an estimation of the total amount of kinetic and 'temperature signal' energies captured by the POD modes as well as the cumulative energy captured by the N^{th} first modes. Accoring to the latter, 61 velocity POD modes and 53 temperature POD modes are required to gather at least 90% of the total energy while modes beyond respectively N=17 and N=15 carry less than 1% of the total energy.

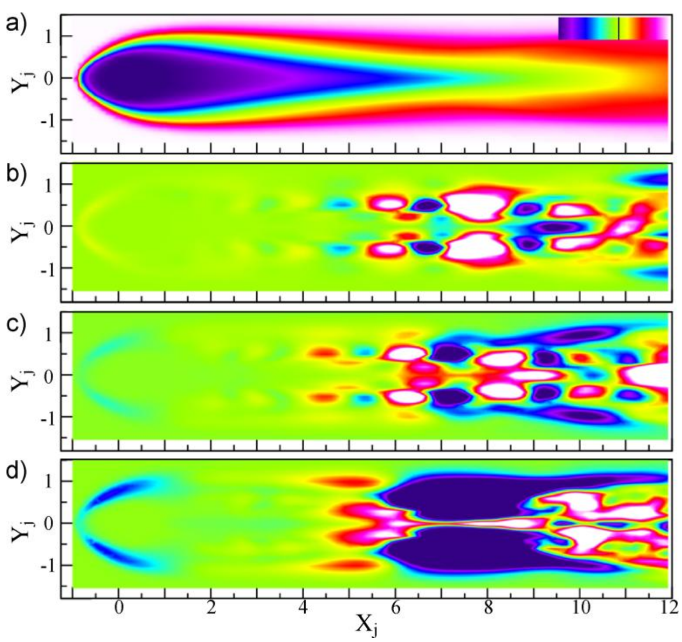

Figure 17 – Mean temperature field and first significant temperature POD modes at BR=0.15 a) Mode0; b) Mode1; c) Mode2; d) Mode5. Slices Z_j=0 with temperature contours.

In Fig. 18 an instantaneous velocity field was reconstructed from truncated POD series to assess the number of modes necessary to rebuild the dominant flow features. In the plane Y_j=0, the first reconstruction using only 2 modes does not render the formation of the individual hairpin vortex present in the original snapshot at X_j=10.6. This is due to the absence of information carried by higher order modes with respect to the hairpin vortices as seen in Fig. 11l, thus justfying the lack of accuracy of the reconstructed field. The individual hairpin vortex is observed for $N_r \geq 8$. In the near field of the jet (X_j<6) the reconstruction appears relatively close to the original field with as few modes as 8, due to the low fluctuation levels and limited length scales of the structures in this region. In the plane X_j=6 however, the features of the original flow such as the two counter rotating vortices located at Z_j=0.3, Y_j=±1 are only consistently reconstructed for $N_r \geq 20$. Similarly in the plane X_j=10.6, the location and scale of the multiple structures present in the original snapshot are only captured in reconstructions including 20 modes or more. Overall, although closer from the actual snapshot, the reconstruction using 60 modes does not appear to constitute a significant improvement over the one with 20 modes in terms of the dominant features.

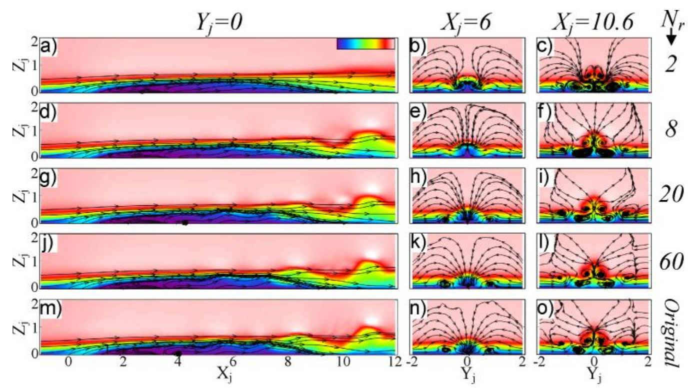

Figure 18 – Reconstructed velocity field for multiple values of N_r. Stream traces correspond to in-plane velocity, contours to streamwise velocity.

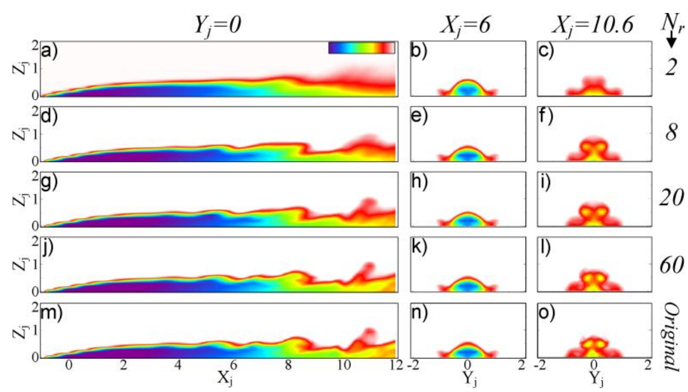

Figure 19 – Reconstructed temperature field for multiple values of N_r.

Figure 19 shows reconstructed and original temperature fields corresponding to Fig. 18. Overall in the plane Y_j=0, the reconstructed temperature field appears to render individual structures beyond N_r=8, with a relativelly satisfying definition for $N_r \geq 20$. Similarly, in the planes X_j=6 and X_j=10.6, the reconstructed fields show very little differences.

Beyond the qualitative examination of the reconstructed fields, time averaged error distributions with respect to the original field were also calculated to assess the quantitative accuracy obtained with a given number of POD modes. For the velocity field, the error in local kinetic energy. This choice has the advantage of combining all three velocity components into a single figure of merrit in addition of being directly related to the norm used for the orthogonal decomposition. However, as the 0^{th} mode corresponds to the time averaged velocity field, not carrying any intrinsic error, it appears more adequate to monitor the error on the turbulent kinetic energy (TKE) rather than the total kinetic energy. The errors distributions on the turbulent kinetic energy are presented in Fig. 20. In the plane Y_j=0, two zones can be identified. Beyond X_j=6 the error on the decreases significantly to be almost zero for N_r=60. However for X_j<6, the error, although decreasing, stays significant in the jet shear layers even with as many as 100 POD modes. It should also be noted that the extent of this zone of relativelly high error decreases with increasing number of POD modes included in the decomposition. This can be explained by the nature of the proper orthogonal decomposition and the norm associated with it imposing a hierarchy of the modes based on the amount of kinetic energy they capture so that the first modes will capture the large scale structures of the domain. In the current study, the principal instability responsible for the formation of the shear layer hairpin vortices is of the convective type and exhibits multiple length scales as it develops in the downstream direction to reach maximum intensity in the far-field. The POD modes thus capture first the downstream motion carrying the largest amount of energy and then progressivelly capture the lower shear layer fluctuations by going in a reverse direction to the development of the instability thus justifying the relatively poor quality of the recontruction in the near field of the jet. This constitutes one of the limitations of the standard POD which may lead to dynamical innaccuracy when trying to implement a reduced order model of the flow as pointed out by [35].

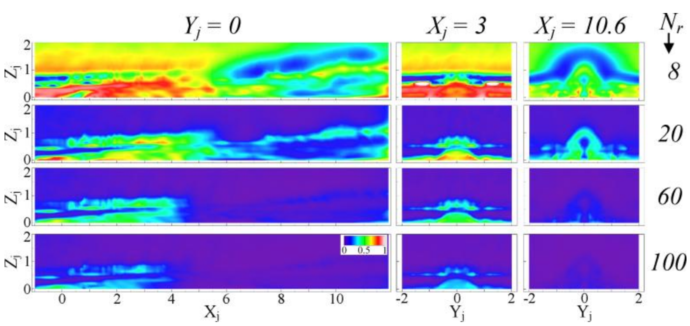

Figure 20 – Average TKE error of the reconstructed fields for various values of N_r. Max. contour value 1 (*white*).

Since no pertubation on the temperature field was imposed at the inlets of the domain and by nature the energy equation is free of an explicit non-linear term in T capable of producing or sustaining fluctuations, in a large part of the domain the true temperature fluctuation is extremely low, even null, and thus induced extremely high errors on the fluctuation value when monitoring the reconstructed temperature field. Based on these considerations, it was decided to monitor the absolute relative error on the total temperature field rather than the fluctuation part, reported in Fig. 21. The error on the temperature field decreases consistently with increasing number of POD modes included in the reconsruction. Most of the error is concentrated beyond X_j=5 where most of mixing and temperature fluctuations occur. It should be noted that similarly to the turbulent kinetic energy, the error in the shear layer of the near-field, appears to decrease at a slower rate than in the far-field. Overall with N_r=20, the maximum error was found to be inferior to 2%, decreasing to less than 1% with N_r=60.

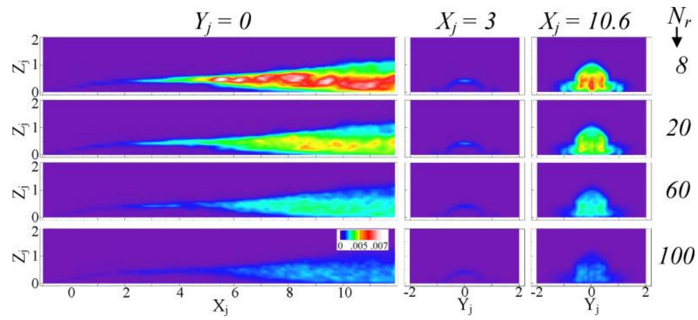

Figure 21 – Average temperature error of the reconstructed field at various N_r values. Max. contour value: $7e^{-3}$ (*white*).

CONCLUSION

Part I of this study focused on the behavior of unforced inclined jets in cross-flow as a baseline for forced jets. In unforced conditions, it was observed that the inclined jet behaved similarly to the vertical configuration with different jet regimes associated to distinct vortical structures. Special attention was brought to the attached configuration, more relevant to film cooling, and the principal vortical structures as well as their impact on the wall temperature field. In agreement with previous work, it was observed that coverage and adiabatic effectiveness performance of the inclined jet in laminar boundary layer cross-flow conditions was comparable to that of the vertical jet, within the limited domain considered, although greater spread for the former resulted in overall better performance.

3D proper orthogonal decomposition of both velocity and temperature fields was carried out on a steady state case at BR=0.15. The most energetic velocity POD modes were found to be associated with the convection of the shear layer vortices encountered at this blowing ratio while higher order modes accounted for their interaction with side vortices located near the wall. The temperature analysis led to a more convoluted decomposition due to the non-optimality of the norm associated to standard POD. The reconstruction of both fields has shown that satisfactory results can be obtained by including a total of 20 POD modes. However, due to the nature of the proper orthogonal decomposition, the relative error in the vicinity of the jet exit remains high and could potentially affect the behavior of a reduced order model based on a truncated series.

In Part II [15] of the current study, forced jets will be analyzed in a similar way to the unforced ones and compared to the baseline results presented in Part I.

ACKNOWLEDGMENTS

The authors would like to thank the Air Force Office of Scientific Research for supporting this work under grants FA9550-06-1-0335 and FA9550-08-1-0440 as well as the Louisiana Board of Regents for supporting an instrumentation enhancement through grant LEQSF(2006-07)-ENH-TR-14.

REFERENCES

[1] Nikitopoulos, D. E., Oertling, J., Acharya, S., and F, M. "On Active Control of Film-Cooling Flows," *ASME Turbo Expo: Power for Land, Sea and Air*. Barcelona, Spain, 2006.

[2] Ekkad, H. "Recent Development in Turbine Blade Film Cooling," *International Journal of Rotating Machinery* Vol. 7, No. 1, 2001, pp. 21-40.

[3] Bunker, R. S. "A Review of Shaped Hole Turbine Film-Cooling Technology," *Journal of Heat Transfer* Vol. 127, No. 4, 2005, pp. 441-453.

[4] Bell, C. M., Ligrani, P. M., Hull, W. A., and Norton, C. M. "Film cooling subject to bulk flow pulsations: effects of blowing ratio, freestream velocity, and pulsation frequency," *International Journal of Heat and Mass Transfer* Vol. 42, No. 23, 1999, pp. 4333-4344.

[5] Ligrani, P. M., Gong, R., Cuthrell, J. M., and Lee, J. S. "Bulk flow pulsations and film cooling--II. Flow structure and film effectiveness," *International Journal of Heat and Mass Transfer* Vol. 39, No. 11, 1996, pp. 2283-2292.

[6] Ligrani, P. M., Gong, R., Cuthrell, J. M., and Lee, J. S. "Bulk flow pulsations and film cooling--I. Injectant behavior," *International Journal of Heat and Mass Transfer* Vol. 39, No. 11, 1996, pp. 2271-2282.

[7] Womack, K. M., Volino, R. J., and Schultz, M. P. "Measurements in Film Cooling Flows With Periodic Wakes," *Journal of Turbomachinery* Vol. 130, No. 4, 2008, pp. 041008-13.

[8] Narayanan, S., Barooah, P., and Cohen, J. M. "Dynamics and Control of an Isolated Jet in Crossflow," *AIAA Journal* Vol. 41, No. 12, 2003, pp. 2316-2320.

[9] M'Closkey, R. T., King, J. M., Cortelezzi, L., and Karagozian, A. R. "The actively controlled jet in crossflow," *Journal of fluid Mechanics* Vol. 452, 2002, pp. 325-335.

[10] Ekkad, S., Ou, S., and Rivir, R., B. "Effect of Jet Pulsation and Duty Cycle on Film Cooling From a Single Jet on a Leading Edge Model," *Journal of Turbomachinery* Vol. 128, No. July 2006, 2006, pp. 564-571.

[11] Coulthard, S. M., Volino, R. J., and Flack, K. A. "Effect of Jet Pulsing on Film Cooling-Part I: Effectiveness and Flow-Field Temperature Results," *Journal of Turbomachinery* Vol. 129, No. 2, 2007, pp. 232-246.

[12] Coulthard, S. M., Volino, R. J., and Flack, K. A. "Effect of Jet Pulsing on Film Cooling-Part II: Heat Transfer Results," *Journal of Turbomachinery* Vol. 129, No. 2, 2007, pp. 247-257.

[13] Womack, K. M., Volino, R. J., and Schultz, M. P. "Combined Effects of Wakes and Jet Pulsing on Film Cooling," *Journal of Turbomachinery* Vol. 130, No. 4, 2008, pp. 041010-12.

[14] Bidan, G., Oertling, J., Boulladoux, P. E., and Niktopoulos, D. E. "Experimental and numerical study of a steady and modulated transverse jets at low blowing ratios," *ASME TurboExpo*. Glasgow, Scottland, 2010.

[15] Bidan, G., Vezier, C., and Niktopoulos, D. E. "Study of steady and modulated inclined film cooling jets using proper orthogonal decomposition – Part II: Forced jets," *ASME TurboExpo*. Vancouver, Canada, 2011.

[16] Burd, S. W., Kaszeta, R. W., and Simon, T. W. "Measurements in Film Cooling Flows: Hole L/D and Turbulence Intensity Effects," *Journal of Turbomachinery* Vol. 120, No. 4, 1998, pp. 791-798.

[17] Goldstein, R. J., Eckert, E. R. G., and Burggraf, F. "Effects of hole geometry and density on three-dimensional film cooling," *International Journal of Heat and Mass Transfer* Vol. 17, No. 5, 1974, pp. 595-607.

[18] Lutum, E., and Johnson, B. V. "Influence of the Hole Length-to-Diameter Ratio on Film Cooling With Cylindrical Holes," *Journal of Turbomachinery* Vol. 121, No. 2, 1999, pp. 209-216.

[19] Acharya, S., and Tyagi, M. "Large Eddy Simulation of Film Cooling Flow From an Inclined Cylindrical Jet," *ASME Conference Proceedings* Vol. 2003, No. 36886, 2003, pp. 517-526.

[20] Guo, X., Schröder, W., and Meinke, M. "Large-eddy simulations of film cooling flows," *Computers & Fluids* Vol. 35, No. 6, 2006, pp. 587-606.

[21] New, T. H., Lim, T. T., and Luo, S. C. "Elliptic jets in cross-flow," *Journal of fluid Mechanics* Vol. 494, No. -1, 2003, pp. 119-140.

[22] Fric, T. F., and Roshko, A. "Vortical structure in the wake of a transverse jet," *Journal of Fluid Mechanics* Vol. 279, 1994, pp. 1-47.

[23] Kelso, R. M., Lim, T. T., and Perry, A. E. "An experimental study of round jets in cross-flow," *Journal of Fluid Mechanics* Vol. 306, 1996, pp. 111-144.

[24] Yuen, C. H. N., and Martinez-Botas, R. F. "Film cooling characteristics of a single round hole at various streamwise angles in a crossflow: Part I effectiveness," *International Journal of Heat and Mass Transfer* Vol. 46, No. 2, 2003, pp. 221-235.

[25] Rowley, C. W., Colonius, T., and Murray, R. M. "Model reduction for compressible flows using POD and Galerkin projection," *Physica D: Nonlinear Phenomena* Vol. 189, No. 1-2, 2004, pp. 115-129.

[26] Moreno, D., Krothapalli, A., Alkislar, M. B., and Lourenco, L. M. "Low-dimensional model of a supersonic rectangular jet," *Physical Review E* Vol. 69, No. 2, 2004, p. 026304.

[27] Cavar, D., Meyer, K. E., Jakirlić, S., and Šarić, S. "LES Based POD Analysis of Jet in Cross Flow." 2010, pp. 253-259.

[28] Meyer, K. E., Pedersen, J. M., and Özcan, O. "A turbulent jet in crossflow analysed with proper orthogonal decomposition," *Journal of fluid Mechanics* Vol. 583, No. -1, 2007, pp. 199-227.

[29] Vernet, R., Thomas, L., and David, L. "Analysis and reconstruction of a pulsed jet in crossflow by multi-plane snapshot POD," *Experiments in Fluids* Vol. 47, No. 4, 2009, pp. 707-720.

[30] Sirovich, L. "Turbulence and the dynamics of coherent structures. Part I: Coherent structures.," *Quaterly Applied Mathematics* Vol. 45, No. 3, 1987, pp. 561-671.

[31] Bernsdorf, S., Rose, M. G., and Abhari, R. S. "Modeling of Film Cooling---Part I: Experimental Study of Flow Structure," *Journal of Turbomachinery* Vol. 128, No. 1, 2006, pp. 141-149.

[32] Gunes, H., and Rist, U. "Spatial resolution enhancement/smoothing of stereo--particle-image-velocimetry data using proper-orthogonal-decomposition--based and Kriging interpolation methods," *Physics of Fluids* Vol. 19, No. 6, 2007, pp. 064101-19.

[33] Gunes, H. "Low-dimensional modeling of non-isothermal twin-jet flow," *International Communications in Heat and Mass Transfer* Vol. 29, No. 1, 2002, pp. 77-86.

[34] Liakopoulos, A., Blythe, P. A., and Gunes, H. "A Reduced Dynamical Model of Convective Flows in Tall Laterally Heated Cavities," *Proceedings: Mathematical, Physical and Engineering Sciences* Vol. 453, No. 1958, 1997, pp. 663-672.

[35] Ilak, M., and Rowley, C. W. "Modeling of transitional channel flow using balanced proper orthogonal decomposition," *Physics of Fluids* Vol. 20, No. 3, 2008, pp. 034103-17.

